

Article

Monitoring-System Development for a Bottom-Set Gillnet through Time-Domain Dynamic Simulations

Chungkuk Jin ^{1,*} , HanSung Kim ¹, Moo-Hyun Kim ¹ and Kiseon Kim ²

¹ Department of Ocean Engineering, Texas A&M University, Haynes Engineering Building, 727 Ross Street, College Station, TX 77843, USA; goldwatch@naver.com (H.K.); m-kim3@tamu.edu (M.-H.K.)

² School of Electrical Engineering and Computer Science, Gwangju Institute of Science and Technology, 123 Cheomdangwagi-ro, Buk-gu, Gwangju 61005, Korea; kskim@gist.ac.kr

* Correspondence: kenjin0519@gmail.com; Tel.: +1-979-204-3454

Received: 6 March 2019; Accepted: 19 March 2019; Published: 22 March 2019



Abstract: This paper investigates the sensor-based monitoring feasibility of a bottom-set gillnet through time-domain dynamic simulations for various current and wave conditions and failure scenarios. The dimension and design parameters of the bottom-set gillnet were based on an existing model used in Korea, and the measured environmental data were acquired from the southwest coast of Korea and utilized for the dynamic analysis. For efficient numerical modeling of nets, an equivalent net model which uses fewer line elements was considered, and the projected area, wet weight, and axial stiffness were accordingly adjusted. The hydrodynamic forces on the entire gillnet were estimated using a Morison-force model on the instantaneous positions of the net. The designed gillnet provided excellent stretching performance even under low current velocity. The dynamic responses under wave excitations were not significant in operating conditions; however, significant motions were observed in the fishery-prohibition condition. The proposed monitoring system consisted of an accelerometer, tension sensors, and the global positioning system. Numerous line-failure scenarios were simulated, and the proposed monitoring system could effectively detect a specific problem from the combined patterns of sensor signals by a problem-detection algorithm.

Keywords: fishing gear; bottom-set gillnet; computer simulation; dynamic analysis; equivalent net model; numerical sensor; monitoring system; failure scenarios; problem-detection algorithm

1. Introduction

In recent decades, marine-environmental pollution from lost fishing gear has been regarded as a serious problem [1]. In particular, one technical report showed that 20% of fishing gear in Korea is lost or abandoned, and within this amount, only roughly 15% is collected [2]. This means that the remaining 85% may be problematic to the marine environment. Therefore, cost-effective methods to prevent the loss of fishing gear is necessary, and developing an economical and functional monitoring system can be a solution.

Since a net system is fully submerged and cannot be directly observed, the monitoring system has to use sensors. For this, the underwater dynamic behaviors of a net system must be well understood for a sensor-based monitoring system for fishing gear to be designed. In this regard, the utilization of a reliable numerical-simulation tool is essential for analyzing overall dynamic behaviors of various types of fishing cages/gear in site-specific environmental conditions. Morison-force [3–13] and screen-force [14,15] models are the two popular approaches used to analyze fishing gears and nets. In particular, the Morison-force model has been validated with experiments in current and wave conditions. Lee et al. [4] have suggested a numerical model for a fishing cage with a floating collar and have compared their results with experiments. Huang and Pan [5] investigated a single-point

mooring (SPM) cage system to investigate the fatigue of a mooring line under wave and constant current loads. Zhao et al. [6] conducted experiments for a gravity cage and compared hydrodynamic behaviors of the cage and mooring tensions with numerical simulations in waves and currents. Furthermore, the dynamic behaviors of box- and column-shaped net cages under wave excitations and steady currents were compared through experiments and numerical simulations by Zhao et al. [7]. Floater-net coupled dynamic analyses in currents and waves have been performed by Cifuentes and Kim [8] and Chen and Christensen [9]. Cifuentes and Kim [10] provided a detailed method for developing a cruder, equivalent net model in their time-domain numerical analysis and compared their numerical results, including a wake model, for downstream nets in currents with experiments. Moreover, Cifuentes and Kim [11] have further validated their numerical methods for net dynamics and mooring tensions in currents and waves with experiments. Xu et al. [12] studied the hydrodynamic behaviors of a four-cage-coupled system including a comparison between simulations and experiments. Jin et al. [13] conducted time-domain analyses of a stow net in various current velocities and wave heights and investigated the feasibility of the monitoring system for fishing gears. Authors of [8,10,11,13] have presented many comparisons against various experimental results to consistently validate the developed time-domain simulation tool for various types of nets and cages.

In this study, a bottom-set gillnet, which is one of the most widely used types of fishing gear in Korea [16], was selected. A bottom-set gillnet generally consists of a long, slender net (also defined as the net assembly in this study), mooring lines and ropes, and location buoys. Floats and weights are added along the head and ground ropes so that it can stand vertically in the water. The invisible net catches fish while traveling without them being aware of it; thus, stretching performance in the vertical direction is an essential factor in the net design. Also, mooring lines with heavy anchors are located at a specified interval to maintain the position of the net. Location buoys float on the sea surface during operation to visually show the location of the net.

The primary purpose of this study was to reliably simulate the dynamic behaviors of the bottom-set gillnet in different current and wave conditions and to develop a cost-effective sensor-based monitoring system that can detect various failures of the bottom-set gillnet. The monitoring system may also be applied to protect fishing gear in case of deep-water turbulences. Even though there have been experiments [17,18] and numerical simulations [19,20] investigating the dynamic behaviors of the gillnet, these have only focused on small sections of the gillnet. This means that there has been no publication in the open literature which has attempted to investigate not only the global behaviors of the bottom-set gillnet but also the simulations of transient responses with various scenarios of line failures, which could be applied to the development of a sensor-based monitoring system. A commercial program, OrcaFlex, was used as a base program and the entire gillnet was rigorously modeled through equivalent line elements and three degrees of freedom (DOF) buoys. Previous studies have included authors' well validated methodologies for the similar applications of fishing cages/gear under waves and currents [3–13]; thus, in this study, we adopted those procedures for dynamic analysis. Since the longitudinal length of a bottom-set gillnet can be up to several kilometers, creating an equivalent net model is essential in modeling, and the equivalent net model was completed by adjusting the projected area, wet weight, and axial stiffness. The relative-velocity-based Morison-force model, which has been suggested by previous research [3–13], was applied at the instantaneous net-position to estimate the hydrodynamic force on the entire system, which is also critical in simulating highly transient phenomena. The global performance of the bottom-set gillnet was investigated in operational and fishery-prohibition conditions. Particularly, in this study, various failure scenarios and the corresponding patterns of numerical sensors were further analyzed for the feasibility of the sensor-based monitoring system. Key monitoring parameters were identified to detect sudden failures of mooring lines and location-buoy-connection ropes. Furthermore, using real-time sensor signals, a simple monitoring algorithm was devised and demonstrated as an example of machine-based problem-detection and decision-making processes.

2. Numerical Model

2.1. Configuration

Figure 1 shows a schematic view of the entire bottom-set-gillnet system and the net assembly utilized in this study. The numerical models of the gillnet were based on an actual design used in Korea and the design parameters and material properties used in this study, given in Table 1, were obtained from previous research [21,22]. As mentioned before, the entire bottom-set gillnet consisted of the net assembly, mooring lines, and location buoys. The net assembly, which was made of nylon monofilament, had a length and height of 300 m and 2 m, respectively. The hanging ratio, which is defined as the actual gillnet length divided by the fully stretched length, is considered as an essential factor in catching fish, and a widely used value of 0.5 [23] was adopted in the present study. In the net assembly, many floats and weights were fixed to head and ground ropes at equal intervals of 0.5 m. Wood bars were positioned at fixed intervals of 50 m along the net-assembly length to maximize the stretching performance of the net assembly. The mooring lines were made of polypropylene and secured by strong anchors. They were installed at intervals of 50 m to maintain the location of the net assembly. The original purpose of the location buoy was to check the location of the underwater portion of the gillnet visually since they float on the sea surface. Each location buoy was connected to the net assembly through a polypropylene rope, and three location buoys were installed at 150 m intervals. The water depth was set as 25 m. The net bottom almost touched the seabed.

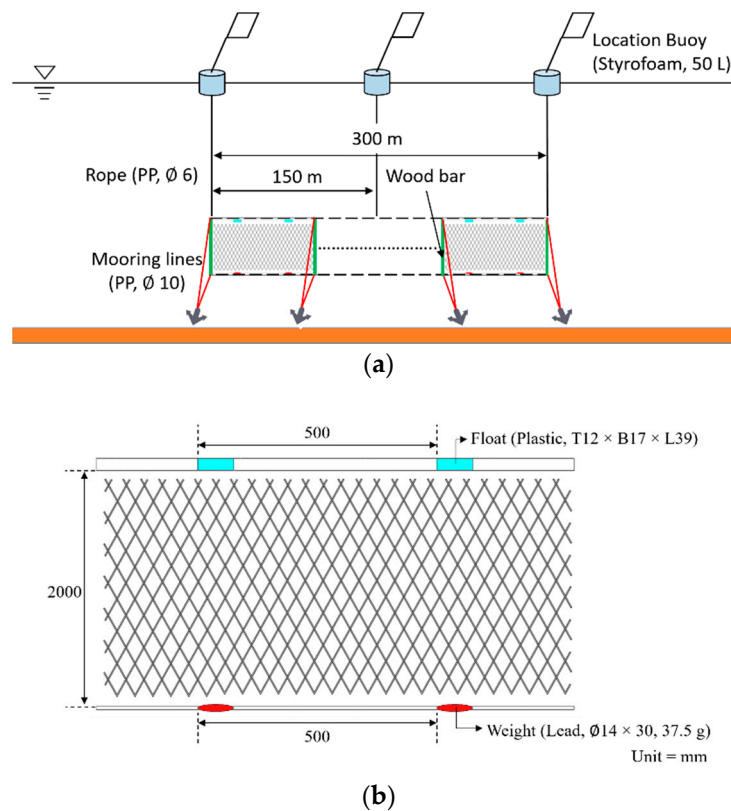


Figure 1. 2D views of entire bottom-set gillnet (a) and the net assembly (b).

Table 1. Material properties and design parameters.

Item		Value	Unit
Net	Length	300	m
	Height	2	m
	Material	Nylon monofilament	-
	Diameter	0.25	mm

Table 1. Cont.

Item		Value	Unit
Head and ground ropes, mooring lines	Material Diameter	Polypropylene 10	- mm
Floats	Material Volume	Plastic $12 \times 17 \times 39$	- mm^3
Weights	Material Size (volume)	Lead $\phi 14 \times 30$	- mm^3
	Mass	37.5	g
Buoys	Material Size	Styrofoam 50	- L

2.2. Time-Domain Numerical Simulation

The bottom-set gillnets were numerically modeled using OrcaFlex, a well-known commercial program [24]. In this study, the gillnet models were entirely created using line and 3-DOF-buoy models, as shown in Figure 2. A 3-DOF-buoy model was introduced for modeling other components such as floats, weights, and location buoys, as well as a convenient connection of line models. The Morison-force model for a moving object was employed to estimate the external force of the entire gillnet. In the Morison equation, the added mass coefficient was fixed as 1.0 for the entire line model [25], which corresponded to an inertia coefficient of 2.0. The Morison forces were calculated at each time step at the members' instantaneous locations and inclinations using the instantaneous normal cross-flow relative velocities and accelerations. The drag coefficient for the net should represent the physical net well, and the formulation suggested by DeCew et al. [26] was adopted in this study. On the other hand, the drag coefficient for mooring lines and ropes was fixed as 1.2 [27]. The equations and detailed descriptions can be found in Jin et al. [13].

Creating an equivalent net model is one of the most important parts of developing a numerical model. If the numerical model is to realize the physical net as it is, significant computational time is unavoidable due to the massive number of lines and 3-DOF-buoys that may represent connecting knots. Thus, to reduce the number of line and buoy elements, an equivalent net model is needed, which is much more efficient in terms of modeling and computational time. In the present study, the wet weight as well as the projected area were matched between the physical and numerical nets. When the projected area was matched to produce equivalent viscous drag forces, the numerical net became heavier and stiffer than the physical net. The heavier numerical net was compensated for by changing the buoyancy in the 3-DOF-buoy model used to connect line models. In addition, the issue related to larger axial stiffness can be solved by introducing a modified Young's modulus, as discussed by Fredheim [28]. The inertial force term has a much smaller magnitude compared with the drag force term considering the large value of the Keulegan-Carpenter (KC) number and given wave conditions [29]. In this case, the inertial force term in the Morison equation can be neglected. Cifuentes and Kim [10] have thoroughly explained the detailed procedure used to develop an equivalent net model. Except for the net, the other components were modeled as they are. For the convergence-test purpose, two numerical models, which are a cruder model (Model A), as presented in Figure 2, and a finer model (Model B), are created. Model A is made up of 568-line and 308 3-DOF-buoy models while Model B has 1831-line and 971 3-DOF-buoy models.

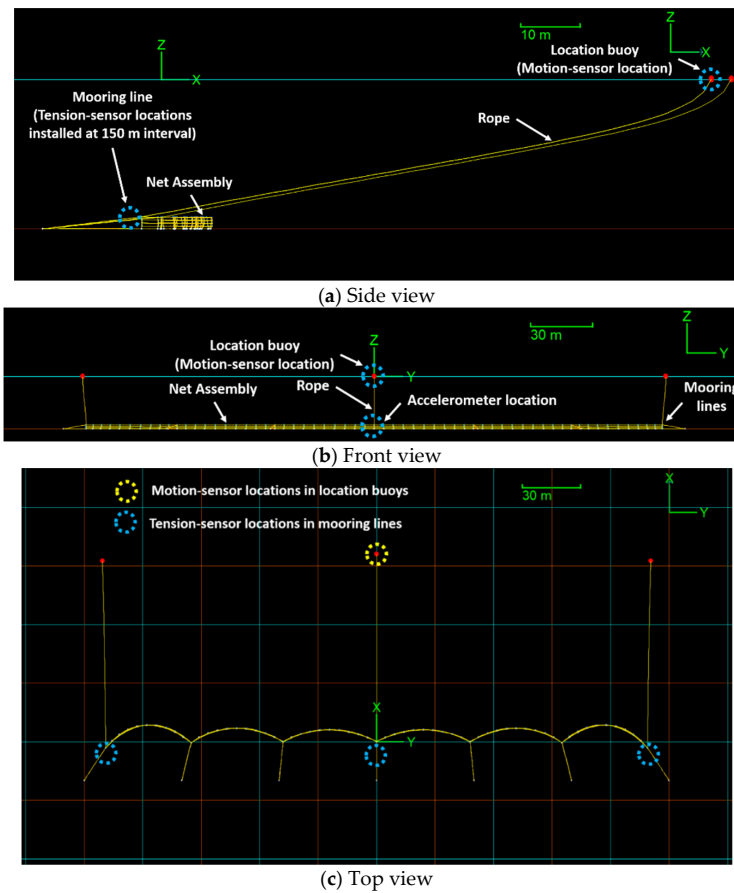


Figure 2. Side (a), front (b), and top (c) views of the designed numerical model of the bottom-set gillnet.

3. Environmental Conditions

Table 2 summarizes the environmental conditions used in this study. The measured current and wave data, acquired in the southwest coast of Korea for three years, were utilized in this study. The corresponding probabilities of current velocity, significant wave height (H_s), and peak period (T_p) had been analyzed by the authors of [13] in previous research. The operating conditions were selected from the analyzed data. Moreover, the fishery-prohibition condition in Korea, which is a significant wave height of 5 m, was additionally simulated to observe the corresponding global performance of the system [30]. A JONSWAP wave spectrum was utilized to generate irregular-wave time histories. In the operating conditions, the enhancement parameter was fixed as 1.0, which is the same as in the Pierson-Moskowitz wave spectrum. Furthermore, an enhancement parameter of 2.14 for the fishery-prohibition condition was based on the average value of the Korean site [31]. A current profile was produced by the power-law method. The current velocity at the bottom was assumed to be 10% of the free-surface-current velocity. Waves and currents were linearly superposed where their nonlinear interaction effects were not considered. The directions of waves and currents were collinear and were fixed to a positive x -axis (0 degrees). Detailed descriptions for wave and current generations can be found in Jin et al. [13].

Table 2. Wave and current conditions for the parametric study.

Wave and Current Conditions				
Significant wave height, H_s (m)	1.0	2.0	3.0	5.0
Peak period, T_p (s)	6.0	7.0	8.0	10.0
Enhancement parameter, γ	1.0	1.0	1.0	2.14
Surface current velocity (m/s)	0.2 ...	0.4 ...	0.6 ...	0.8 ... 1.0

4. Convergence Test

When the equivalent net model was used, it was essential to check its convergence by varying the numbers of lines and 3-DOF-buoys. In this regard, the results of the less fine Model A and the much-finer Model B were compared to show that both models produce similar results. Recall that Model B has approximately three times more lines and 3-DOF-buoys compared to Model A. Figures 3 and 4 show the envelopes of the lateral (X direction) and vertical (Z direction) motions of the net assembly of Models A and B at a current velocity of 0.6 m/s. Figure 5 shows mooring tensions at the middle location with current velocities from 0.2 m/s to 1.0 m/s. Waves were not considered in the convergence test. Model A produced almost the same motion results, both in the lateral and vertical directions, compared to Model B. In addition, there were no significant differences in the mooring tensions between the two. The maximum difference in mooring tensions was only 3.2 percent for the top mooring line at a current velocity of 0.4 m/s. Since the computational time of Model B was ten times more than that of Model A, while both produced almost the same results, Model A was repeatedly used to produce the ensuing results from this point on to investigate the global performance of the system.

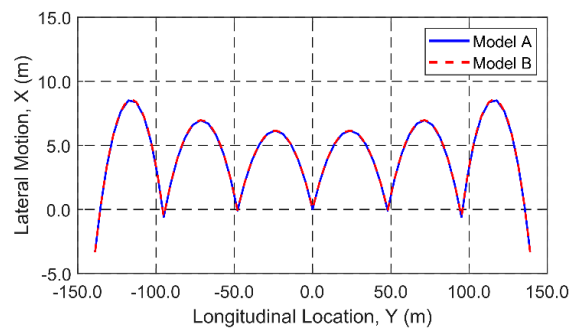


Figure 3. Envelopes of lateral motions ($Z = -23$ m) of Model A and Model B at a current velocity of 0.6 m/s for the convergence test.

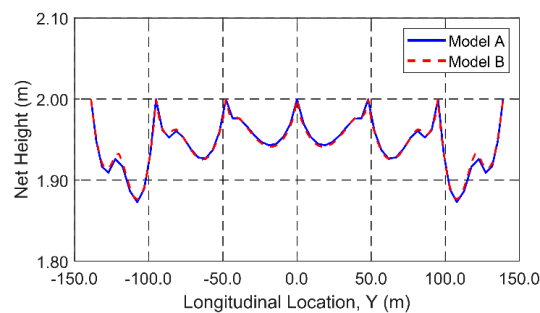


Figure 4. Envelopes of vertical motions (net-top motion minus net-bottom motion) of Model A and Model B at a current velocity of 0.6 m/s for the convergence test.

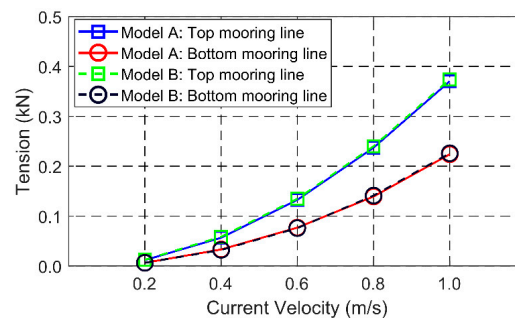


Figure 5. Convergence test: mooring tensions of Model A and Model B at the middle location with different current velocities.

5. Global Performance of the Bottom-Set Gillnet

5.1. Effects of Current Velocity

Figure 6 shows the lateral-response envelopes of the net assembly at various current velocities. Waves were not considered in this section to observe the effects of constant-current velocity. Generally, the net assembly stretched well between respective anchors/mooring lines for the given current-velocity range. Except for the current velocity of 0.2 m/s, lateral envelopes were almost the same because mooring lines maintained the net position tightly without any more extension. Figure 7 presents the envelopes of the net heights at diverse current velocities. Current velocity greatly influences net height, and, generally, the higher the current velocity, the lower the net height without wood bars [17,32,33]. However, in the present net system, the net height was maintained well due to the adoption of wood bars, as shown in Figure 7. As mentioned before, wood bars were located in the net assembly at 50 m intervals. Because of these wood bars, the net heights around the wood bars kept their original net height of 2.0 m while reductions were observed between them. The most substantial reduction in net height was observed at the smallest current velocity of 0.2 m/s since too low current velocity results in less drag force to stretch the net assembly fully; however, its reduction was not significant. In addition, net-height reduction at high current velocities was largely improved by the existence of wood bars. In other words, the net assembly was well stretched in the vertical direction at all current velocities, mainly due to the wood bars. In conclusion, the designed bottom-set gillnet showed excellent stretching performance in the lateral and vertical directions across a typical range of current velocity. In addition, as shown in Figure 5, mooring tensions increased with current velocity because of the increased drag forces on the gillnet. Higher mooring tensions were observed in top mooring lines because current velocity decreases with submergence depth.

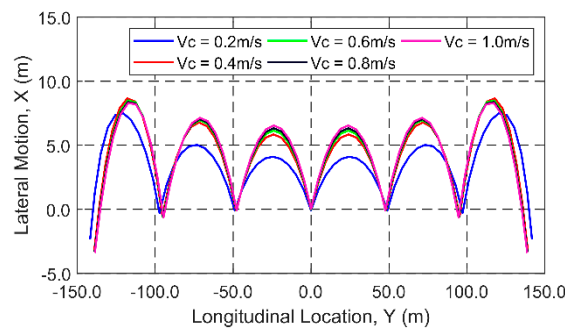


Figure 6. Envelopes of the lateral responses ($Z = -23$ m) of the net assembly at different current velocities.

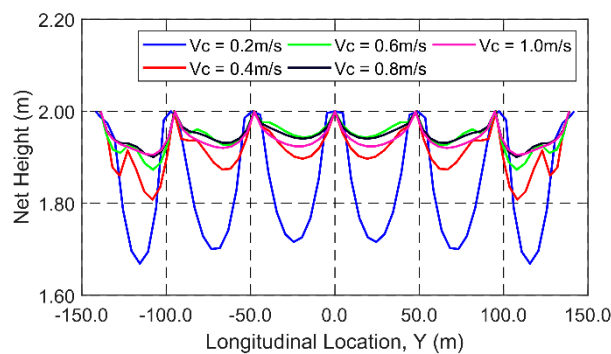


Figure 7. Envelopes of the vertical responses (net-top motion minus net-bottom motion) of the net assembly at different current velocities.

5.2. Effects of Wave Excitations

Figures 8 and 9 present the time histories of the lateral and vertical responses at the middle location ($Y = 0.0$ m, $Z = -23.0$ m) in different wave conditions and their envelopes for the significant wave height (H_s) of 5.0 m. The wave and current directions were in the X direction, i.e., perpendicular to the net plane. In this section, the rope length was 100 m and the current velocity was set as 0.6 m/s. Figures 8a and 9a show that the net dynamics were small in typical operating conditions, i.e., H_s was less than 2.0 m. However, in the fishery-prohibition condition ($H_s = 5.0$ m), significant fluctuations were noticed, and their amplitudes increased more than the linear increase. As shown in Figures 8 and 9, the lateral motions were usually more significant in the negative direction than in the positive direction (direction of wave and current) because mooring tensions could more effectively restrict the positive-direction responses. The maximum lateral response was observed in the location between mooring lines because the highly flexible net assembly was free to move there. The vertical responses were, on the other hand, mostly in the positive direction, since the bottom of the net almost touched the seabed. They had the largest values at the positions of mooring lines due to the effects of wood bars and rope tensions. The mooring lines hardly restricted the vertical motions because the mooring lines were almost lateral, i.e., perpendicular to the net plane. The vertical responses between mooring lines were significantly coupled with lateral concaved responses since the net was flexible.

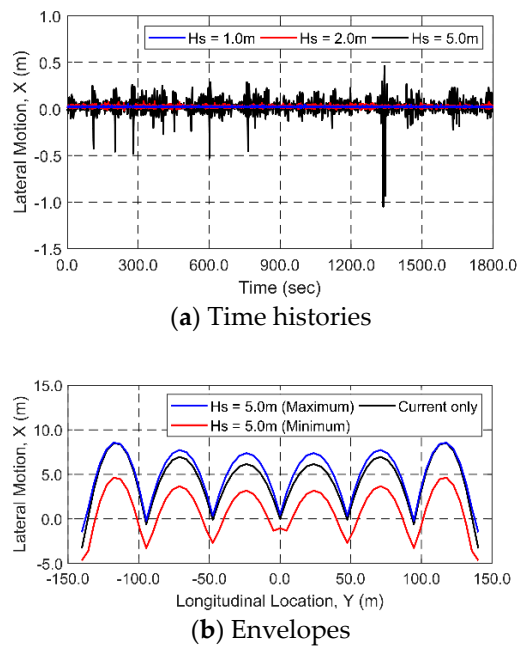


Figure 8. Time histories of the lateral motions of the net at the top-middle location ($Y = 0$ m, $Z = -23$ m) under different wave conditions (a) and motion envelopes along the net length at $H_s = 5.0$ m and $T_p = 10.0$ s (b) (current velocity = 0.6 m/s).

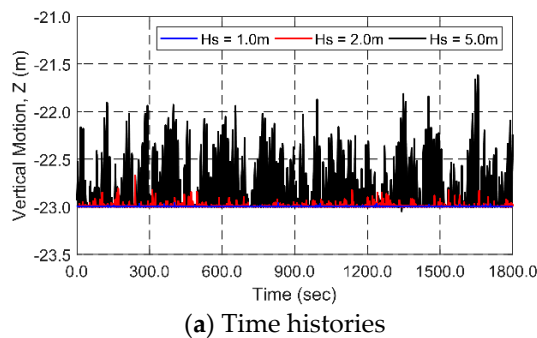


Figure 9. Cont.

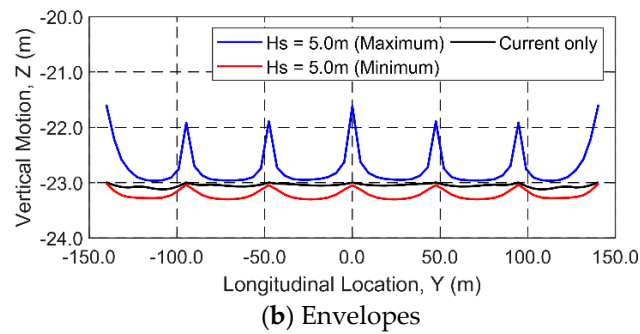


Figure 9. Time histories of the vertical motions of the net at the top-middle location ($Y = 0$ m, $Z = -23$ m) in different wave conditions (a) and motion envelopes along the net length at $H_s = 5.0$ m and $T_p = 10.0$ s (b) (current velocity = 0.6 m/s).

Figure 10 shows the time histories of the mooring tension at the mooring line located in the upper center under different wave conditions and the corresponding distribution of mooring tension along the length for an H_s of 5.0 m, considered to be the fishery-prohibition condition. Again, the fluctuations in mooring tensions were small when H_s was less than 2.0 m, whereas mooring tensions were significantly amplified for $H_s = 5.0$ m. The high mooring tension under this fishery-prohibition condition was mainly caused by the sudden increase of tension by snap loading after the mooring line was slack. In this slack-taut repeating scenario, not only can mooring lines be broken, but also, anchors can be dragged out in harsh waves and strong currents. Progressive failures of mooring lines can happen after one mooring line is broken.

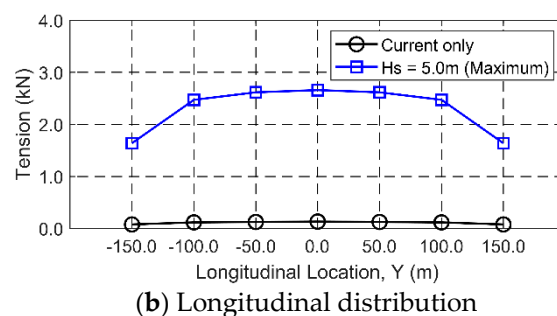
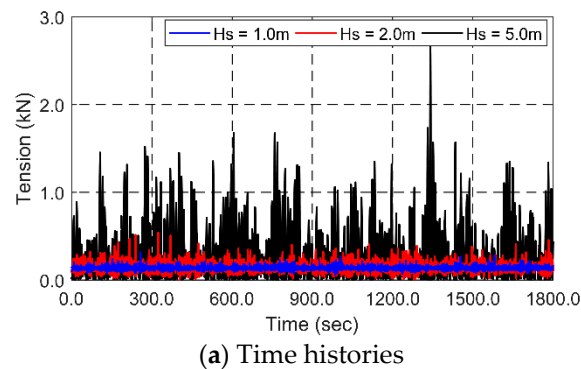


Figure 10. Time histories of the mooring tension at the middle location (top mooring line) under different wave conditions (a) and the corresponding spatial distribution along the net length at $H_s = 5.0$ m and $T_p = 10.0$ s (b) current velocity = 0.6 m/s.

6. Identification of Monitoring Parameters in Line-Failure Scenarios

In this section, the monitoring parameters in different line-failure locations were identified. Of course, installing more sensors would have provided better accuracy of failure monitoring; however,

considering the cost of the entire bottom-set gillnet, this was unfeasible. Therefore, finding key monitoring parameters was required. In this regard, the limited number of sensors were located in the net assembly, the location buoy, and mooring lines, as shown in Figure 2. In particular, an accelerometer was installed in the center location of the net assembly to measure accelerations in 3 DOFs, a global positioning system (GPS) was attached to a location buoy in the center to measure displacements in 3 DOFs, and tension sensors were positioned at the top mooring lines at the center and end locations of the net assembly. Since the GPS measures motions of the buoy, real-time wave statistics, e.g., significant wave height and peak period, could be acquired by solving the inverse problem using a Kalman filter, which has been done by other authors [34]. Authors have proven that the real-time inverse estimation of ocean waves from heave sensor signals using an adaptive Kalman-filter technique successfully reproduces the real-time wave elevations and spectra. The proposed physical system had 14 mooring lines, and critical parameters to detect failure scenarios were investigated. Additionally, a rope connecting the net assembly to a location buoy could be broken, and hence the effect of the rope failure was also checked.

A GPS cannot deliver its signal in the water; thus, it is necessary for the buoy not to be fully submerged during operation. Besides, if the length of the rope is too short, it can cause significant vertical motions of the net by the heave motions of the location buoy. These considerations needed to be investigated before key-parameter identifications. Figure 11 shows the time histories of the dry length (or freeboard), which was defined as the instantaneous length of a buoy (volume = 50 liters) above the water surface at different rope lengths. An H_s and T_p of 2 m and 7 s, respectively, were applied. It was seen that the rope length significantly influenced the dry length of the location buoy. When the rope was short, the interaction between the net assembly and the location buoy was significant, i.e., the short rope could more easily pull down the location buoy. On the other hand, for a long slack rope, the interaction between the net and buoy became weaker, resulting in smaller variations of freeboard.

Figure 12 shows the time histories of the vertical motion of the net assembly in the middle location. A case without location buoys was also simulated to check the importance of the interaction between the buoy and the net assembly. Due to the significant interaction between the net assembly and the location buoy, significant vertical motions occurred when the rope length was 50 m. However, the interaction effect became weaker when the rope length was increased. The vertical motions for the proposed design with 100 m rope length were similar to those without location buoys. In conclusion, the proposed location-buoy and rope designs with 100 m length were able to locate the GPS sensor with a view to minimizing buoy-net interactions and maintaining the buoy's freeboard.

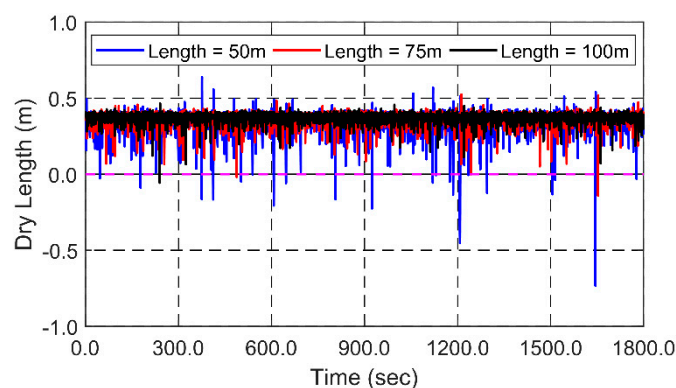
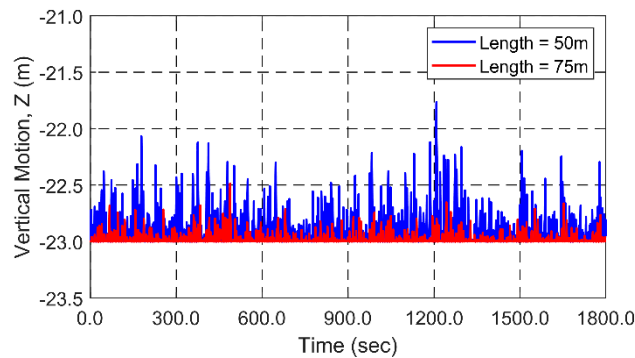
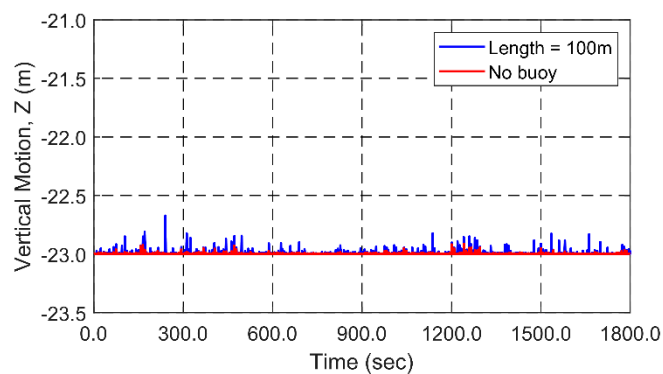


Figure 11. Time histories of the dry length of the location buoy in the middle location for $H_s = 2.0$ m, $T_p = 7.0$ s, and current velocity = 0.6 m/s (the pink line is a reference level which the dry length should be higher than to prevent the buoy from being fully submerged).



(a) Rope lengths of 50 m and 75 m



(b) Rope length of 100 m and no buoy or rope

Figure 12. Time histories of the vertical motion of the net assembly at $Y = 0$ m, $Z = -23$ m in the middle location for $H_s = 2.0$ m, $T_p = 7.0$ s, and current velocity = 0.6 m/s (the bottom-set gillnet without location buoys was also simulated for comparison).

Figures 13–15 show the time histories of mooring tensions, surge motions of the location buoy, and X-Y directional accelerations of the net assembly in the middle location (height center $Z = -24$ m) as mooring lines in the middle location ($Y = 0$ m) were broken after 600 s. The three scenarios—top mooring failure, bottom-mooring failure, and both failures—were investigated for $H_s = 2.0$ m and $T_p = 7.0$ s. For other wave cases, only statistical data have been presented. In the case of the top mooring line being broken, the corresponding mooring tension became zero since a tension sensor was located there. When the bottom mooring line broke, the mean value and standard deviation of the top-mooring tension increased, as shown in Figure 13. In the case of both mooring lines being broken, the tension-sensor reading became zero, while the surge motion of the location buoy increased by approximately 20.0 m, as presented in Figures 13 and 14. The X-directional accelerations abruptly changed with failure due to the transient impulsive response at the moment of failure. The signal also showed larger variations after failure; however, Y-directional accelerations did not change appreciably after failure happens, as shown in Figure 15, since the symmetry of the system in the Y direction was maintained. Therefore, for each failure scenario, there existed a unique combination of sensor-signal changes, which could be used for data-based problem-detection and decision-making processes.

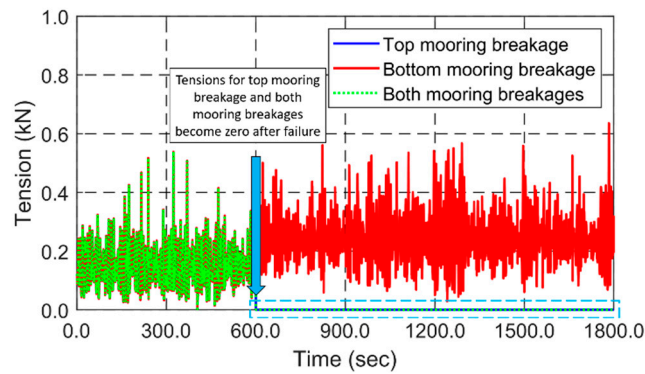


Figure 13. Time histories of the mooring tension in the middle location ($Y = 0$ m) as mooring lines in the middle location ($Y = 0$ m) are broken after 600 s ($H_s = 2.0$ m, $T_p = 7.0$ s, current velocity = 0.6 m/s).

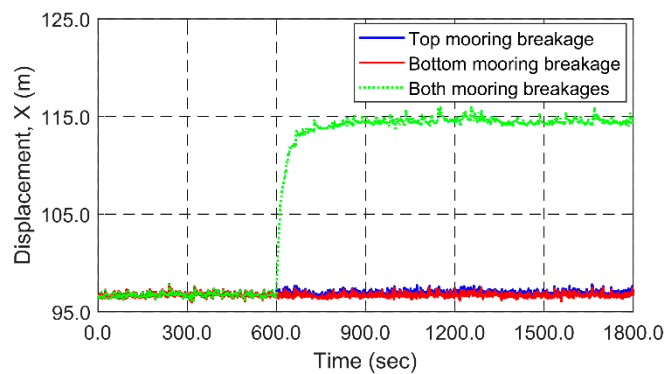


Figure 14. Time histories of the surge motion of the location buoy in the middle location ($Y = 0$ m) as mooring lines in the middle location ($Y = 0$ m) are broken after 600 s ($H_s = 2.0$ m, $T_p = 7.0$ s, current velocity = 0.6 m/s).

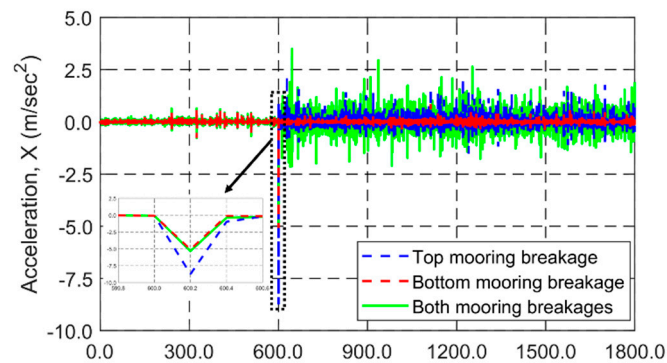


Figure 15. Cont.

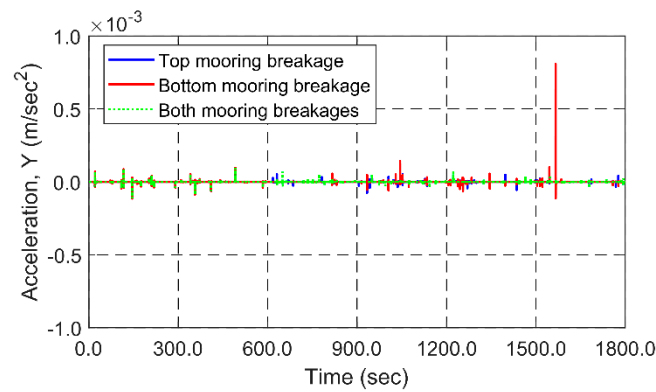


Figure 15. Time histories of the X (**top**) and Y (**bottom**) directional accelerations of the net assembly in the middle location ($Y = 0$ m) as mooring lines in the middle location ($Y = 0$ m) are broken after 600 s ($H_s = 2.0$ m, $T_p = 7.0$ s, current velocity = 0.6 m/s).

Figures 16 and 17 show the time histories of mooring tensions and X-Y directional accelerations of the net assembly in the middle location (at $Y = 0$ m) as mooring lines at $Y = -50$ m are broken after 600 s. In this case, both the X- and Y-directional accelerations show transient impulsive peaks at the moment of line failure. The transient peak in the Y direction occurs because the Y-directional symmetry is suddenly lost. After the line failure, both the center-mooring tensions and Y-directional accelerations appreciably increased due to the increased dynamics as a result of the loss of neighboring lines. When those two previous line-failure events are compared, the sensor-signal patterns become quite distinct, and each failure scenario can be identified by observing the behavior of the sensor signals. Similar simulations and analyses have been carried out for other mooring-line-failure scenarios and the critical parameters for failure detection are summarized in Table 3. Additional simulated statistical data for different wave conditions are also presented in Tables 4–6.

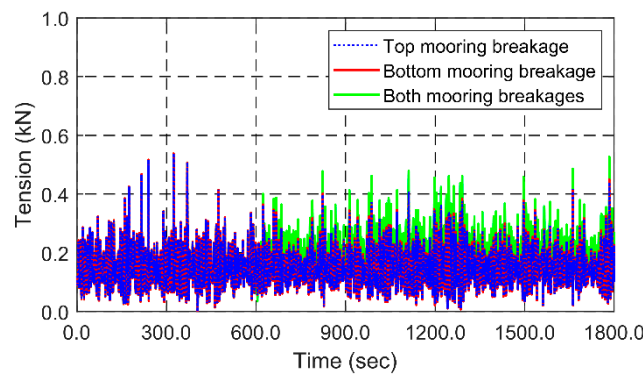


Figure 16. Time histories of the mooring tension in the middle location ($Y = 0$ m) as mooring lines at $Y = -50$ m are broken after 600 s ($H_s = 2.0$ m, $T_p = 7.0$ s, current velocity = 0.6 m/s).

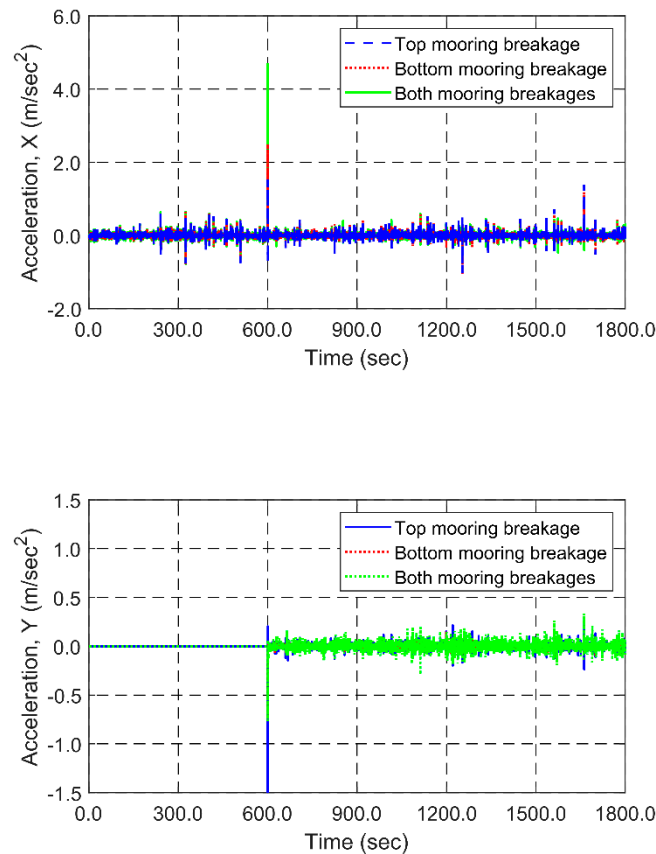


Figure 17. Time histories of X (top) and Y (bottom) directional accelerations of the net assembly in the middle location ($Y = 0\text{ m}$) as mooring lines at $Y = -50\text{ m}$ are broken after 600 s ($H_s = 2.0\text{ m}$, $T_p = 7.0\text{ s}$, current velocity = 0.6 m/s).

Table 3. Key monitoring parameters in different mooring-line-breakage scenarios (TEN = tension of top mooring line, DX = surge motion of location buoy in the middle location of the net assembly, AX = X-directional acceleration in the middle location of the net assembly, AY = Y-directional acceleration in the middle location of the net assembly, TOP = top mooring line, and BOT = bottom mooring line).

Mooring-Line-Breakage Location		Key Parameters
Y Location	Z Location	
0 m	TOP	TEN ($Y = 0\text{ m}$), AX
0 m	BOT	TEN ($Y = 0\text{ m}$), AX
0 m	TOP and BOT	TEN ($Y = 0\text{ m}$), DX, AX
-50 m	TOP	AY
-50 m	BOT	AY
-50 m	TOP and BOT	AY, TEN ($Y = 0\text{ m}$)
-100 m	TOP	AY
-100 m	BOT	AY
-100 m	TOP and BOT	AY, TEN ($Y = -150\text{ m}$)
-150 m	TOP	AY, TEN ($Y = -150\text{ m}$)
-150 m	BOT	AY, TEN ($Y = -150\text{ m}$)
-150 m	TOP and BOT	AY, TEN ($Y = -150\text{ m}$)

Table 4. Statistical data of mooring tension, surge motion of the location buoy, and acceleration of the net assembly in the X and Y directions in different mooring-line-breakage scenarios at $H_s = 1.0$ m, $T_p = 6.0$ s, and current velocity = 0.6 m/s (AVE = average value and STD = standard deviation).

Mooring-Line-Breakage Location		TEN (Y = 0 m)		TEN (Y = -150 m)		DX (Y = 0 m)		AX (Y = 0 m)	AY (Y = 0 m)
Y Location	Z Location	AVE (kN)	STD (kN)	AVE (kN)	STD (kN)	AVE (m)	STD (m)	STD (m/s ²)	STD (m/s ²)
No breakage		0.138	0.023	0.084	0.016	96.330	0.106	0.033	0.000
0 m	TOP	0.000	0.002	0.084	0.016	96.579	0.105	0.135	0.000
0 m	BOT	0.231	0.025	0.084	0.016	96.341	0.105	0.036	0.000
0 m	TOP and BOT	0.000	0.002	0.090	0.016	113.370	1.690	0.232	0.000
-50 m	TOP	0.138	0.022	0.084	0.016	96.327	0.105	0.067	0.027
-50 m	BOT	0.138	0.022	0.084	0.016	96.327	0.105	0.043	0.010
-50 m	TOP and BOT	0.187	0.026	0.094	0.016	96.309	0.105	0.050	0.018
-100 m	TOP	0.138	0.022	0.085	0.015	96.326	0.105	0.035	0.020
-100 m	BOT	0.138	0.022	0.085	0.015	96.327	0.105	0.034	0.008
-100 m	TOP and BOT	0.140	0.023	0.163	0.024	96.325	0.106	0.034	0.024
-150 m	TOP	0.138	0.023	0.000	0.001	96.326	0.105	0.032	0.029
-150 m	BOT	0.138	0.022	0.138	0.019	96.327	0.105	0.032	0.006
-150 m	TOP and BOT	0.133	0.022	0.000	0.001	96.314	0.105	0.035	0.015

Table 5. Statistical data of mooring tension, surge motion of the location buoy, and acceleration of the net assembly in the X and Y directions in different mooring-line-breakage scenarios at $H_s = 2.0$ m, $T_p = 7.0$ s, and current velocity = 0.6 m/s.

Mooring-Line-Breakage Location		TEN (Y = 0 m)		TEN (Y = -150 m)		DX (Y = 0 m)		AX (Y = 0 m)	AY (Y = 0 m)
Y Location	Z Location	AVE (kN)	STD (kN)	AVE (kN)	STD (kN)	AVE (m)	STD (m)	STD (m/s ²)	STD (m/s ²)
No breakage		0.152	0.066	0.096	0.046	96.713	0.217	0.070	0.000
0 m	TOP	0.000	0.003	0.096	0.045	96.946	0.216	0.264	0.000
0 m	BOT	0.247	0.086	0.096	0.045	96.714	0.211	0.102	0.000
0 m	TOP and BOT	0.000	0.003	0.101	0.045	114.118	1.680	0.397	0.000
-50 m	TOP	0.150	0.061	0.096	0.045	96.700	0.210	0.082	0.042
-50 m	BOT	0.151	0.062	0.096	0.045	96.700	0.210	0.078	0.017
-50 m	TOP and BOT	0.200	0.074	0.105	0.045	96.671	0.210	0.089	0.042
-100 m	TOP	0.151	0.063	0.096	0.043	96.700	0.210	0.074	0.033
-100 m	BOT	0.150	0.062	0.096	0.044	96.700	0.210	0.071	0.016
-100 m	TOP and BOT	0.153	0.063	0.172	0.064	96.692	0.210	0.071	0.047
-150 m	TOP	0.151	0.063	0.000	0.002	96.700	0.210	0.071	0.045
-150 m	BOT	0.151	0.063	0.155	0.062	96.700	0.210	0.071	0.015
-150 m	TOP and BOT	0.146	0.061	0.000	0.002	96.676	0.209	0.068	0.031

Table 6. Statistical data of mooring tension, surge motion of the location buoy, and acceleration of the net assembly in the X and Y directions in different mooring-line-breakage scenarios at $H_s = 3.0$ m, $T_p = 8.0$ s, and current velocity = 0.6 m/s.

Mooring-Line-Breakage Location		TEN (Y = 0 m)		TEN (Y = -150 m)		DX (Y = 0 m)		AX (Y = 0 m)	AY (Y = 0 m)
Y Location	Z Location	AVE (kN)	STD (kN)	AVE (kN)	STD (kN)	AVE (m)	STD (m)	STD (m/s ²)	STD (m/s ²)
No breakage		0.179	0.127	0.116	0.085	96.868	0.265	0.131	0.000
0 m	TOP	0.000	0.003	0.115	0.083	97.154	0.305	0.339	0.000
0 m	BOT	0.289	0.191	0.115	0.083	96.881	0.265	0.201	0.000
0 m	TOP and BOT	0.000	0.003	0.121	0.084	114.518	1.763	0.470	0.000
-50 m	TOP	0.177	0.121	0.115	0.082	96.867	0.266	0.164	0.067
-50 m	BOT	0.178	0.124	0.115	0.082	96.867	0.266	0.164	0.049
-50 m	TOP and BOT	0.232	0.153	0.125	0.087	96.836	0.266	0.129	0.074

Table 6. Cont.

Mooring-Line-Breakage Location		TEN (Y = 0 m)	TEN (Y = -150 m)	DX (Y = 0 m)	AX (Y = 0 m)	AY (Y = 0 m)
-100 m	TOP	0.178	0.124	0.116	0.080	96.867
-100 m	BOT	0.178	0.124	0.116	0.081	96.867
-100 m	TOP and BOT	0.180	0.124	0.197	0.129	96.858
-150 m	TOP	0.178	0.125	0.000	0.002	96.867
-150 m	BOT	0.178	0.125	0.184	0.126	96.867
-150 m	TOP and BOT	0.173	0.121	0.000	0.002	96.833

Finally, Figure 18 shows the time history of the surge motion of the location buoy in the middle location as the connecting rope is broken after 600 s. As is clearly shown in the figure, the surge motion increased continuously due to free drifting on the sea surface. In this case, there should be little changes to other monitoring parameters, simply resulting in the loss of the location buoy, which can easily be fixed. When the whole net is drifting with buoys, fishermen can easily check the location of the gillnet in real time through GPS and collect it.

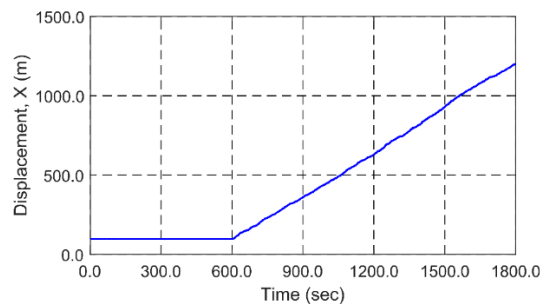


Figure 18. Time histories of the surge motion of the location buoy in the middle location as the rope in the middle location (Y = 0 m) is broken after 600 s ($H_s = 2.0$ m, $T_p = 7.0$ s, current velocity = 0.6 m/s).

Through this kind of computer-simulation tool, a useful big-data set can be generated and machine-based problem-detection or decision-making processes can be established using real-time sensor signals.

7. Example of Monitoring Algorithm

In this section, we demonstrate an example of the machine-based problem-detection algorithm based on sensor signals. Figure 19 shows the developed monitoring algorithm, which was based on the monitoring parameters identified in the previous section. For simplicity, it was assumed that there are four inputs and six outputs. The four inputs were one tension sensor installed at the top of the center-upper-mooring line (Y = 0 m), X-Y accelerometers at the middle height of the net (Y = 0 m), and one displacement sensor on the middle location buoy (Y = 0 m). Since accurate judgment within a time step is difficult, the algorithm detects evidence of abrupt changes within the window by considering continuous small windows of the sensor signals. Mooring lines other than the center one at Y = 0 m are defined as neighboring mooring lines. To check the variation of sensor signals, the average values and standard deviations were continuously obtained inside a small window. To validate the flowchart-based-monitoring algorithm, various failure scenarios were additionally simulated using a wave condition of $H_s = 2.5$ m and $T_p = 7.5$ s. The current was also fixed as 0.6 m/s.

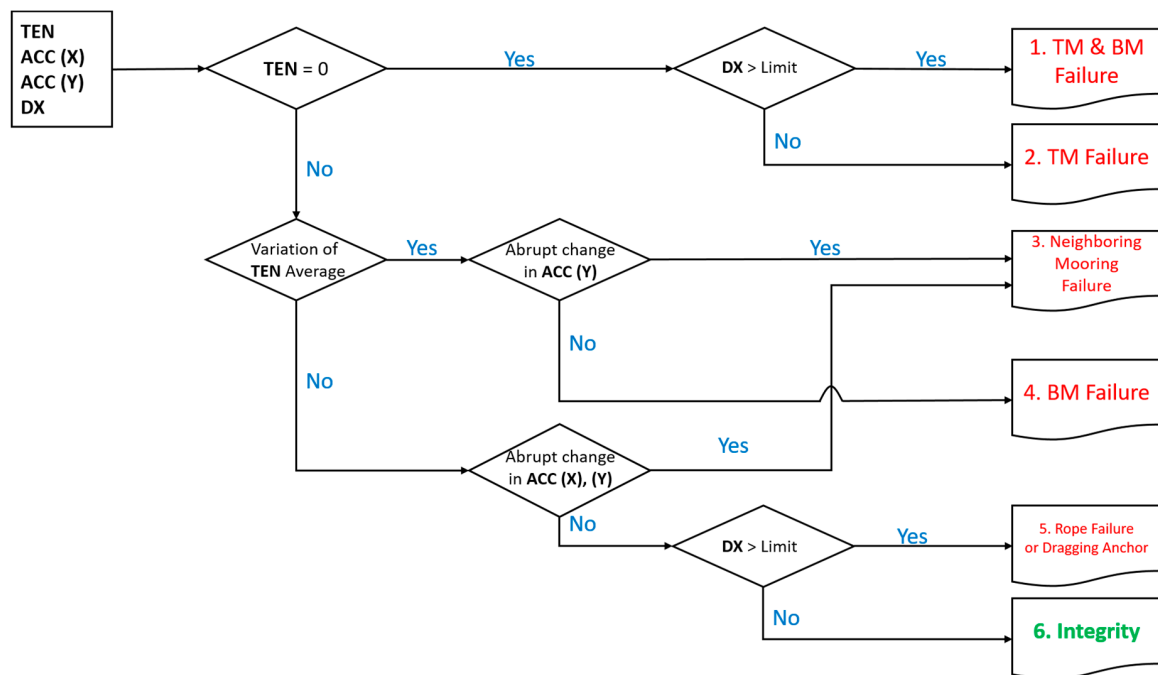


Figure 19. Failure detection algorithm.

Figures 20 and 21 show test results for Output 1 = both mooring lines at $Y = 0$ m are broken and Output 3 = both of the adjacent mooring lines at $Y = -50$ m are broken. The mooring lines were broken after 600 s. Failures were detected well in both cases and the problems were correctly identified. In the case of Output 1, there was a small time lag for detection of about 20 s. The slowly varying surge motion of the location buoy leads to this time delay even if the top mooring tension suddenly became zero. However, the time lag for detecting failure was small, which is acceptable for fishing gear failure monitoring. In the case of Output 3, even though the average value and standard deviation of the mooring tension varied slowly, X and Y accelerations abruptly changed, which resulted in the fast detection of failure even without the time lag. Although not presented here, we tested a number of other failure scenarios, and the developed algorithm was always able to correctly detect and identify the given problem. The overall results demonstrate that the proposed monitoring algorithm can be used for the machine-based problem-detection system of the bottom-set gillnet. A more extensive monitoring system can also be developed with more input and/or output variables.

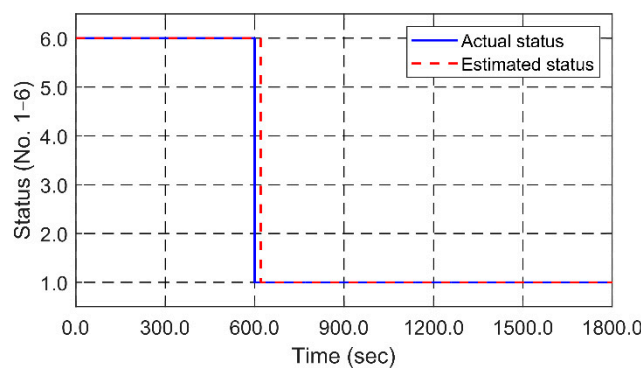


Figure 20. Time histories of failure detection status when both mooring lines in the middle location ($Y = 0$ m) are broken after 600 s ($H_s = 2.5$ m, $T_p = 7.5$ s, current velocity = 0.6 m/s). Status 1 indicates the Output 1 case.

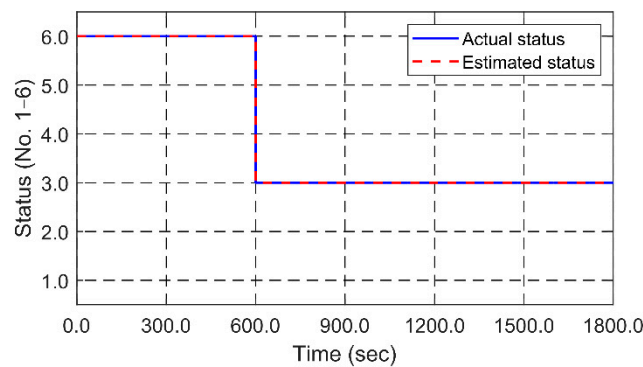


Figure 21. Time histories of failure detection status when both mooring lines at $Y = -50$ m are broken after 600 s ($H_s = 2.5$ m, $T_p = 7.5$ s, current velocity = 0.6 m/s). Status 3 indicates the Output 3 case.

8. Conclusions

In this work, time-domain numerical simulations were performed to analyze the global dynamic performance of a bottom-set gillnet under various current and wave conditions. Simulation tools were developed to design a sensor-based monitoring system and develop the corresponding machine-based problem-detection or decision-making processes. Computer simulations were carried out for a typical range of measure environmental data on the southwest coast of Korea. The target net-system was a bottom-set gillnet constructed by employing an actual design used in Korea. A reliable equivalent net model with Morison forces on instantaneous net/mooring positions was developed. The convergence of the equivalent net model was confirmed by increasing the number of elements used for a finer model. From a series of computer simulations, the following conclusions can be drawn:

- The stretching performance of the gillnet is good under different current loads.
- The effects of wave excitations are small in operating conditions at the given submergence depth. Dynamic responses of the net are, however, substantial in the fishery-prohibition condition, which significantly increases the mooring tension through nonlinear snap loading.
- In different line-failure scenarios, the proposed monitoring system, in combination with three different kinds of sensors, can effectively detect specific problems from the combined patterns of sensor signals.
- The proposed algorithm, based on the analysis of sensor signals and the corresponding statistical data, can be used for failure detection.
- An example of a machine-based problem-detection algorithm using sensor signals has been developed and successfully demonstrated using a number of different failure scenarios.
- In order to develop a more sophisticated algorithm for many different failure cases, big-data analysis combined with machine learning might be a favorable solution.

Author Contributions: All authors contributed equally to the publication of this article with regard to the design of the target model, validation of the numerical model, parametric study, analysis, and writing.

Funding: This research is a part of a project titled ‘Development of Automatic Identification Monitoring System for Fishing Gear’, which is funded by the Ministry of Oceans and Fisheries, Korea.

Conflicts of Interest: The authors declare no conflict of interest.

References

1. Page, B.; McKenzie, J.; McIntosh, R.; Baylis, A.; Morrissey, A.; Calvert, N.; Haase, T.; Berris, M.; Dowie, D.; Shaughnessy, P.D. Entanglement of Australian sea lions and New Zealand fur seals in lost fishing gear and other marine debris before and after government and industry attempts to reduce the problem. *Mar. Pollut. Bull.* **2004**, *49*, 33–42. [[CrossRef](#)] [[PubMed](#)]
2. Lee, K.-N.; An, H.-C. *A Study for Systematic Management of Coastal or Offshore Fishery*; Korea Fisheries Association & National Fisheries Research and Development Institute: Busan, Korea, 2007; pp. 1–334.

3. Bi, C.-W.; Zhao, Y.-P.; Dong, G.-H.; Xu, T.-J.; Gui, F.-K. Numerical simulation of the interaction between flow and flexible nets. *J. Fluids Struct.* **2014**, *45*, 180–201. [[CrossRef](#)]
4. Lee, C.-W.; Kim, Y.-B.; Lee, G.-H.; Choe, M.-Y.; Lee, M.-K.; Koo, K.-Y. Dynamic simulation of a fish cage system subjected to currents and waves. *Ocean Eng.* **2008**, *35*, 1521–1532. [[CrossRef](#)]
5. Huang, C.-C.; Pan, J.-Y. Mooring line fatigue: A risk analysis for an SPM cage system. *Aquac. Eng.* **2010**, *42*, 8–16. [[CrossRef](#)]
6. Zhao, Y.-P.; Li, Y.-C.; Dong, G.-H.; Teng, B.; Gui, F.-K. Numerical simulation of hydrodynamic behaviors of gravity cage in current and waves. *Int. J. Offshore Polar Eng.* **2009**, *19*, 97–107.
7. Zhao, Y.-P.; Gui, F.-k.; Xu, T.-J.; Chen, X.-F.; Cui, Y. Numerical analysis of dynamic behavior of a box-shaped net cage in pure waves and current. *Appl. Ocean Res.* **2013**, *39*, 158–167. [[CrossRef](#)]
8. Cifuentes, C.; Kim, M. Dynamic analysis for the global performance of an SPM-feeder-cage system under waves and currents. *China Ocean Eng.* **2015**, *29*, 415–430. [[CrossRef](#)]
9. Chen, H.; Christensen, E.D. Simulating the hydrodynamic response of a floater–net system in current and waves. *J. Fluids Struct.* **2018**, *79*, 50–75. [[CrossRef](#)]
10. Cifuentes, C.; Kim, M. Numerical simulation of fish nets in currents using a Morison force model. *Ocean Syst. Eng. Int. J.* **2017**, *7*, 143–155.
11. Cifuentes, C.; Kim, M. Hydrodynamic response of a cage system under waves and currents using a morison-force model. *Ocean Eng.* **2017**, *141*, 283–294. [[CrossRef](#)]
12. Xu, T.-J.; Zhao, Y.-P.; Dong, G.-H.; Li, Y.-C.; Gui, F.-K. Analysis of hydrodynamic behaviors of multiple net cages in combined wave-current flow. *J. Fluids Struct.* **2013**, *39*, 222–236. [[CrossRef](#)]
13. Jin, C.; Choi, J.; Kim, M.-H. Response prediction and monitoring feasibility of a stow net system using measured environmental data in the southwest coast of korea. *Appl. Sci.* **2018**, *8*, 1517. [[CrossRef](#)]
14. Kristiansen, T.; Faltinsen, O.M. Modelling of current loads on aquaculture net cages. *J. Fluids Struct.* **2012**, *34*, 218–235. [[CrossRef](#)]
15. Kristiansen, T.; Faltinsen, O.M. Experimental and numerical study of an aquaculture net cage with floater in waves and current. *J. Fluids Struct.* **2015**, *54*, 1–26. [[CrossRef](#)]
16. Park, S.-W.; Kim, S.-H.; Lim, J.-H.; Choi, H.-S. The durability of polybutylene succinate monofilament for fishing net twines by outdoor exposure test. *J. Fish. Mar. Sci. Educ.* **2013**, *25*, 766–774.
17. Stewart, P. Measurements of the effects of tidal flow on the headline heights of bottom-set gillnets. *Fish. Res.* **1988**, *6*, 181–189. [[CrossRef](#)]
18. Savina, E.; Krag, L.A.; Madsen, N.; O'Neill, H.E.F. Developing and testing a computer vision method to quantify 3d movements of bottom-set gillnets on the seabed. *ICES J. Mar. Sci.* **2017**, *75*, 814–824. [[CrossRef](#)]
19. Takagi, T.; Shimizu, T.; Korte, H. Evaluating the impact of gillnet ghost fishing using a computational analysis of the geometry of fishing gear. *ICES J. Mar. Sci.* **2007**, *64*, 1517–1524. [[CrossRef](#)]
20. Wan, R.; Huang, W.; Song, X.; Hu, F.; Tokai, T. Statics of a gillnet placed in a uniform current. *Ocean Eng.* **2004**, *31*, 1725–1740. [[CrossRef](#)]
21. An, Y.-R.; Huh, S.-H. Species composition and seasonal variation of fish assemblages in the coastal waters off gadeok-do, korea 4. Fishes collected by bottom gill nets. *J. Korean Soc. Fish. Technol.* **2003**, *36*, 686–694.
22. Kim, I.-O.; Park, C.-D.; Cho, S.-K.; Kim, H.-Y.; Cha, B.-J. Mesh selectivity of monofilament and multifilament nylon gill net for marbled sole (*Pleuronectes yokohamae*) in the western sea of Korea. *J. Korean Soc. Fish. Technol.* **2010**, *46*, 281–291. [[CrossRef](#)]
23. Gray, C.A.; Broadhurst, M.K.; Johnson, D.D.; Young, D.J. Influences of hanging ratio, fishing height, twine diameter and material of bottom-set gillnets on catches of dusky flathead *platycephalus fuscus* and non-target species in new south wales, Australia. *Fish. Sci.* **2005**, *71*, 1217–1228. [[CrossRef](#)]
24. Orcina. Orcaflex Manual. Available online: <https://www.orcina.com/SoftwareProducts/OrcaFlex/index.php> (accessed on 17 October 2018).
25. Faltinsen, O. *Sea Loads on Ships and Offshore Structures*; Cambridge University Press: London, UK, 1993.
26. DeCew, J.; Tsukrov, I.; Risso, A.; Swift, M.; Celikkol, B. Modeling of dynamic behavior of a single-point moored submersible fish cage under currents. *Aquac. Eng.* **2010**, *43*, 38–45. [[CrossRef](#)]
27. Veritas, D.N. *Offshore Standard dnv-os-e301: Offshore Standard-Position Mooring*; Det Norske Veritas (DNV): Oslo, Norway, 2010.
28. Fredheim, A. Current Forces on Net Structures. Ph.D. Thesis, NTNU, Trondheim, Norway, 2005.

29. Keulegan, G.H. Forces on cylinders and plates in an oscillating fluid. *J. Res. Natl. Bur. Stand. Res. Pap.* **1958**, *2857*, 423–440. [[CrossRef](#)]
30. KMA. Available online: [Http://www.Kma.Go.Kr/help/basic/help_03_02.jsp](http://www.Kma.Go.Kr/help/basic/help_03_02.jsp) (accessed on 21 February 2019).
31. Suh, K.-D.; Kwon, H.-D.; Lee, D.-Y. Some statistical characteristics of large deepwater waves around the korean peninsula. *Coast. Eng.* **2010**, *57*, 375–384. [[CrossRef](#)]
32. He, P. Gillnets: Gear design, fishing performance and conservation challenges. *Mar. Technol. Soc. J.* **2006**, *40*, 12–19. [[CrossRef](#)]
33. Stewart, P.; Ferro, R. Measurements on gill nets in a flume tank. *Fish. Res.* **1985**, *3*, 29–46. [[CrossRef](#)]
34. Kim, H.; Kang, H.; Kim, M. *Real-Time Estimation of Ocean Wave Spectra from Vessel Motion Using Adaptive Kalman Filter, Proceedings of the 29th International Ocean and Polar Engineering Conference, Honolulu, HI, USA, 16 June–21 June 2019*; International Society of Offshore and Polar Engineers: Honolulu, HI, USA, 2019.



© 2019 by the authors. Licensee MDPI, Basel, Switzerland. This article is an open access article distributed under the terms and conditions of the Creative Commons Attribution (CC BY) license (<http://creativecommons.org/licenses/by/4.0/>).